THE JOURNAL OF PHYSICAL CHEMISTRY C

pubs.acs.org/JPCC Article

# Molecular Sensitivity of Near-Field Vibrational Infrared Imaging

Chih-Feng Wang, Bijesh Kafle, Tefera E. Tesema, Hamed Kookhaee, and Terefe G. Habteyes*

Cite This: J. Phys. Chem. C 2020, 124, 21018−21026 Read Online

ACCESS | Metrics & More | Article Recommendations | Supporting Information

**ABSTRACT:** Quantifying the sensitivity limit of scattering-type scanning near-field optical microscopy (s-SNOM) in vibrational infrared imaging requires assembly of molecular systems with continuous variation of height across lateral displacements, which has not been available to date. In this work, we fabricate a film of poly(4-vinylpyridine) (P4VP) with about 7° angle of elevation on gold and silicon substrates and compare the chemical contrast due to the ring stretching vibration of P4VP as a function of sample thickness. We observe that the near-field contrast starts to change at the same time as the sample height, which increases at a rate of a nanometer per 10 nm lateral displacement crossing from the bare substrates to the P4VP-coated region. Saturation of phase contrast is observed for a thicker than 100 nm sample on silicon, while it continues to increase even beyond 200 nm on gold. The presaturation regime on silicon appears to coincide with the higher net field enhancement in the sample on silicon than on gold, in spite of the higher overall scattering amplitude on gold. Although the chemical contrasts are observable as the sample thickness decreases to a sub-nanometer scale on both substrates, important distinctions are observed because of the roughness of the as-prepared gold film. The variation in the local tip−sample geometry results in signal fluctuation that creates uncertainty in the chemical contrast when the sample thickness is comparable to the roughness. The results presented here provide clarity to advance s-SNOM chemical imaging to the molecular "finger print" region of electromagnetic radiation.

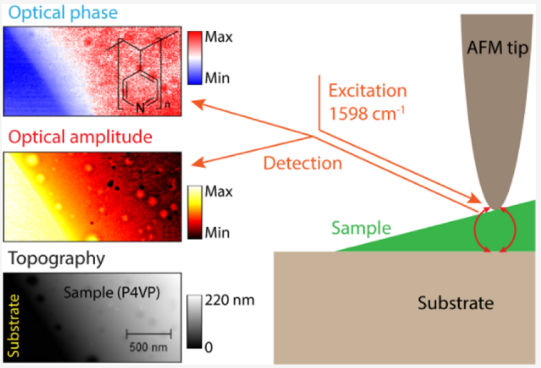




## 1. INTRODUCTION

Infrared (IR) vibrational spectroscopy is one of the most powerful analytical techniques for chemical identification as it probes vibrational transitions that provide "finger print" information about molecular systems. As a result, a microscopic technique that uses IR radiation is suitable for chemical imaging of solid surfaces. For organic molecules, the vibrational transitions are in the wavelength range of 2.7−16.7 $\mu$m, which means that the spatial resolution of a diffraction limited optical microscope will be in the range of several micrometers. The discovery of scattering-type scanning near-field optical microscopy (s-SNOM)[1,2] has provided a viable approach to overcome the diffraction limit and achieve spatial resolution down to a scale of few nanometers, regardless of excitation wavelengths.[3−7] To mention some examples, s-SNOM has been applied for mapping optical modes on metals[6,8−14] and on all-dielectric[15] nanostructures, IR properties of organic thin films[16−18] and proteins,[19,20] plasmon resonances in graphene,[21−24] phonon-polaritons in two-dimensional materials,[25−28] carrier localizations in semiconductors[29−32] and intersubband polaritons in IR nano-antenna.[33]

In s-SNOM measurement, the strength of the near-field signal depends on the optical coupling between the probing tip of the atomic force microscope (AFM) and the sample. For samples with strong oscillators, the sensitivity of s-SNOM is sufficient to map optical modes of atomically thin two-dimensional crystals such as graphene.[21,22,24,34−36] In fact, for imaging of plasmon modes on metal nanostructures, the use of a nonmetallic probe with incident light polarization that does not excite the probe is necessary[10,13,37] to minimize distortion of the inherent optical modes of the sample because of strong tip−sample optical coupling.[14] For molecular systems, on the other hand, the tip−sample optical coupling is weak, and obtaining monolayer sensitivity can be difficult.[38] In particular, the phase contrast that is related to the vibrational absorption resonances[39] can be lost in the background. As a result, in addition to using a metallic tip with excitation field parallel to its axis, it is important to use a strongly polarizable substrate to create large field enhancement at the tip−substrate junction where the sample is placed.[40] However, the field enhancement needed for enhancing the photoabsorption by the sample decreases exponentially with the sample thickness that increases the tip−substrate separation. On the other hand, the absorbance by the sample of interest increases with

Received: September 1, 2020
Published: September 14, 2020

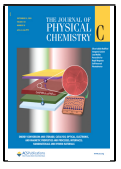





https://dx.doi.org/10.1021/acs.jpcc.0c07979
J. Phys. Chem. C 2020, 124, 21018−21026

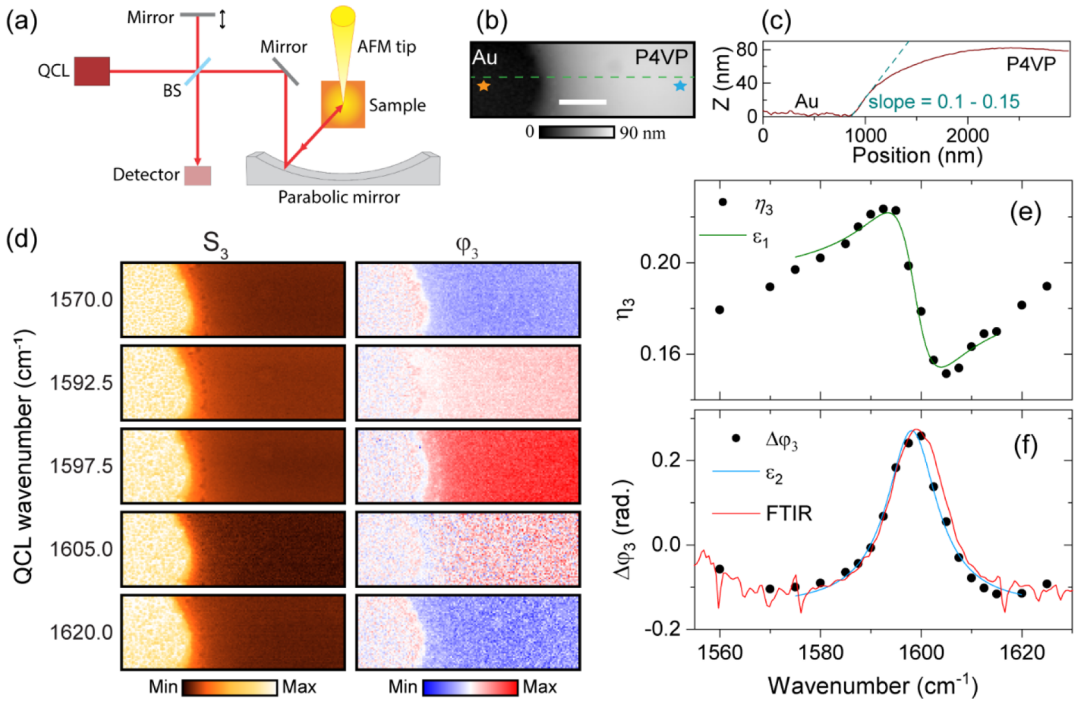


**Figure 1.** Experimental setup and resonance of the P4VP sample. (a) Schematic of the s-SNOM setup. The double-headed arrow by the reference mirror indicates that the mirror is oscillated at ~300 Hz for the pseudoheterodyne interferometric detection. QCL: quantum cascade laser; BS: beamsplitter. (b) Topography of the P4VP on the Au substrate. The scale bar is 500 nm. (c) Line profile across the dashed line on the topography. The slope indicates that the P4VP thickness increases very slowly (not abruptly) starting at the boundary. (d) Representative near-field IR amplitude ($S_3$) and phase ($\varphi_3$) scan images acquired at different excitation wavenumber of the QCL output for the same region shown in the topographic image (b). (e) Spectrum of the relative amplitude (solid circles) and the real part of the P4VP dielectric function fit to the data based on the Lorentzian dipole oscillator (green line). (f) Spectrum of phase difference (solid circles) and the imaginary part of the dielectric function fit to the data (blue line). The red line is normalized FTIR spectrum.

increasing sample thickness. Hence, the molecular signal enhancement due to tip−substrate optical interaction is expected to be limited within a certain sample thickness depending on the nature of the interaction. Modeling the tip as a point dipole, Aizpurua et al. have predicted saturation of optical contrast starting at 35 nm thickness of poly(methyl methacrylate) (PMMA) on gold substrates.[40] More realistic theoretical analysis using finite dipole model indicates that the tip−substrate interaction extends beyond 100 nm.[41] Experimental results that compares enhancement on different substrates have been reported for a poly(ethylene oxide) sample having a thickness of 13 nm using nano-Fourier transform IR (nano-FTIR) spectroscopy, in which the spectra are recorded at a fixed tip position.[42] In another nano-FTIR study of PMMA on gold, the amplitude and phase contrast of different thicknesses (10, 19, 31, and 174 nm) have been compared.[18] However, experimental results that show the variation of amplitude and phase contrasts as a function of sample thickness that increases continuously starting at zero is not available. In other words, the sensitivity limit of s-SNOM vibrational imaging with vanishing sample thickness has not been systematically quantified to date.

In this work, a thin film of poly(4-vinylpyridine) (P4VP) with about 6−8° angle of elevation is prepared on gold and silicon substrates, and the chemical contrasts due to the stretching vibration of the aromatic ring are obtained as a function of film thickness that varies continuously from zero to over 200 nm. We observe that the amplitude and phase contrasts start to change at the same time as the sample thickness starts to increase at a rate of about a nanometer per 10 nm lateral displacement crossing from the bare substrate to the P4VP-coated region. Surprisingly, for sample thickness up to ~100 nm, the phase contrast is slightly higher on Si substrates than on Au. Consistent with the phase contrast, our analysis indicates higher net field enhancement for the sample on Si, in contrast to the significantly larger overall scattering amplitude on Au. Saturation of phase contrast is observed starting at ~100 nm of sample thickness on Si, while the contrast continues to increase even beyond 200 nm on the Au substrate. On both substrates, it is possible to discern the overall chemical contrast as the sample thickness decreases to a sub-nanometer scale. However, important distinctions are observed between the chemical contrasts on the two substrates owing to the roughness of the gold surface. As the sample thickness becomes comparable to the surface roughness of Au, the signal fluctuation due to the tip−substrate local coupling geometry can overwhelm the chemical contrast. The results presented here may serve as a benchmark to search for appropriate substrates to improve the sensitivity of chemical imaging using s-SNOM that does not require fabrication of specialized probes.

## 2. METHODS

**2.1. Sample Preparation.** The P4VP sample is prepared on P-doped N-type silicon ⟨100⟩ wafer (UniversityWafer, Inc.) and a gold film of ~100 nm thickness. The gold film is prepared through electron-beam deposition of gold on the silicon wafer using 2 nm titanium as an adhesion layer. The P4VP sample with a thickness gradient is prepared by solution drop-casting that is followed by spin-coating at slow speed.


https://dx.doi.org/10.1021/acs.jpcc.0c07979
J. Phys. Chem. C 2020, 124, 21018−21026

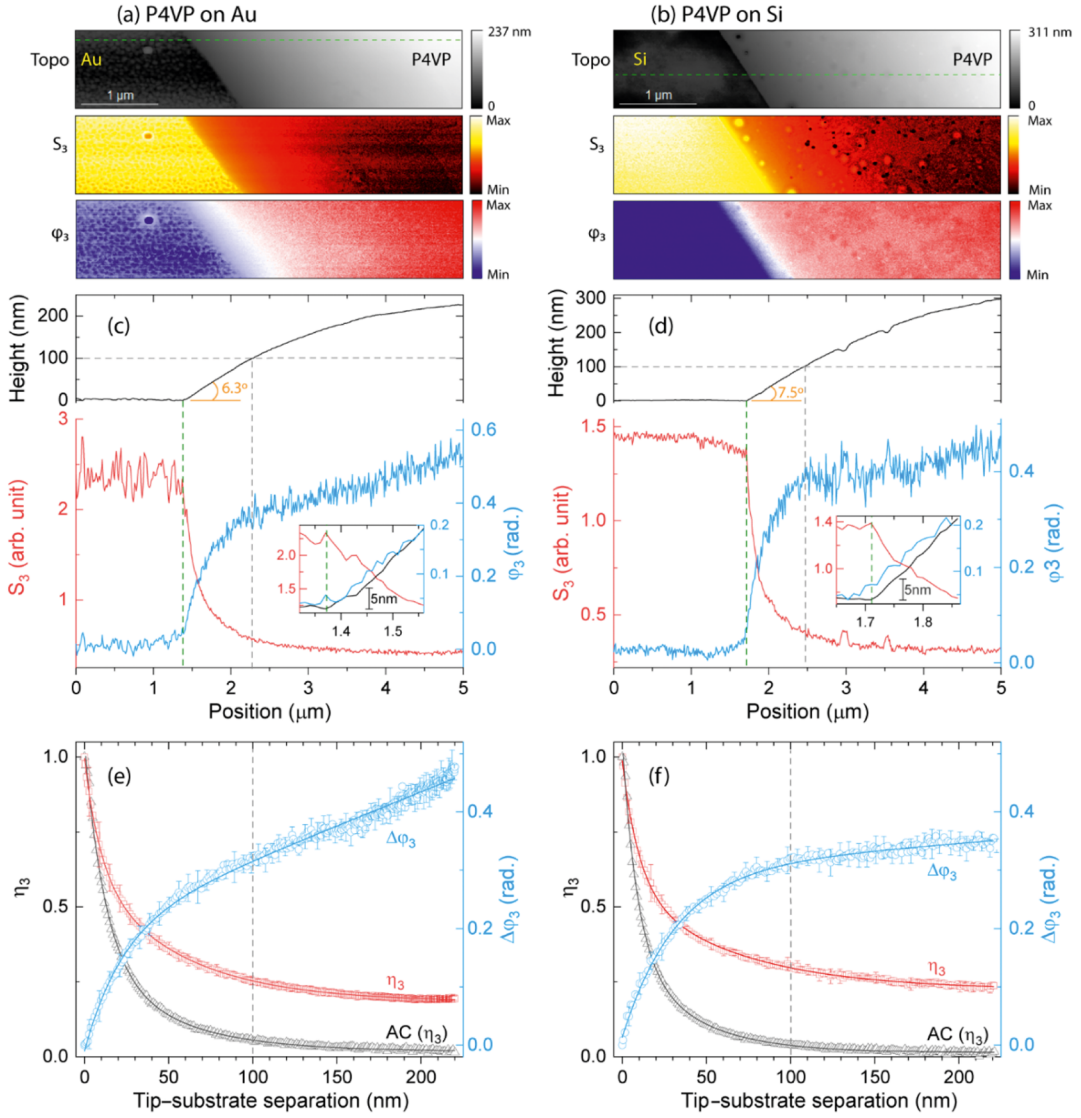


**Figure 2.** Comparison of vibrational near-field contrast on Au and Si substrates at a P4VP resonance frequency of 1598 $cm^{-1}$. Simultaneously recorded topography, near-field amplitude ($S_3$) and near-field phase ($\varphi_3$) scan images of P4VP on (a) Au and (b) Si substrates. Line profiles of the topography (black line), near-field amplitude (red line), and near-field phase (blue line) for the images on (c) Au and (d) Si substrates. The magnified plots in the inset show the transition at the boundary. (e,f) Near-field amplitude (red squares, left axis), AC, (black triangles, left axis) and phase (blue circles, right axis) as a function of tip−substrate separation (or P4VP thickness) on (e) Au and (f) Si substrates. The solid lines are biexponential functions fit to the data. The near-field amplitude as a function of P4VP thickness and AC are normalized (see the raw data in Figure S2a,b).

That is, about 10 $\mu$L of a 0.2 wt % P4VP solution in ethanol is applied on a clean substrate at room temperature, and then spin-coating is performed immediately at a speed of 200 rpm for 5 min using a commercial spin-coater (Laurell Technologies Co., model WS-650MZ-23NPP). This procedure resulted in P4VP film covering only some portion of the substrate with a clear boundary between the P4VP-coated and bare substrate, as can be seen in scan images of the film on gold and silicon in Figures S1. A thickness gradient with 6−8° angle of elevation is obtained going from the boundary into the P4VP-covered region of the substrate. In addition, ultrathin P4VP film on gold is prepared by spin-coating 500 $\mu$L of 0.2 wt % P4VP/ethanol solution at a speed of 6000 rpm for 4 min. Then, some portion of the film is immersed in isopropanol for 1 s to create a boundary of bare Au and P4VP-Au.

**2.2. Near-Field Measurement.** The near-field optical amplitude and phase contrasts of P4VP on gold and silicon substrates are obtained using the commercial Neaspec AFM /near-field platform that implements the pseudoheterodyne interferometric detection procedure,[43] as shown by the schematic in Figure 1a. Using the output of a quantum cascade laser (MIRcat, Daylight Solutions), the excitation frequency is tuned in the 1570−1620 $cm^{-1}$ range to cover the aromatic ring stretching vibration frequency of P4VP. The laser power is adjusted to ∼3 mW as measured before the beam splitter of the interferometer. A commercially available metal-coated AFM tip (Arrow NCPt, NanoWorld) is used as a near-field probe at a tapping frequency ($\Omega$) of ∼270 kHz and tapping amplitude of ∼70 nm. The signal scattered by the tip is mixed with the reference beam and is focused onto the HgCdTe IR detector (Kolmar, KLD-0.25-J1). The output of the detector is demodulated at $m\Omega$ ($m \geq 1$), and the signals obtained at $m$ = 2−4 are compared.


https://dx.doi.org/10.1021/acs.jpcc.0c07979
J. Phys. Chem. C 2020, 124, 21018−21026

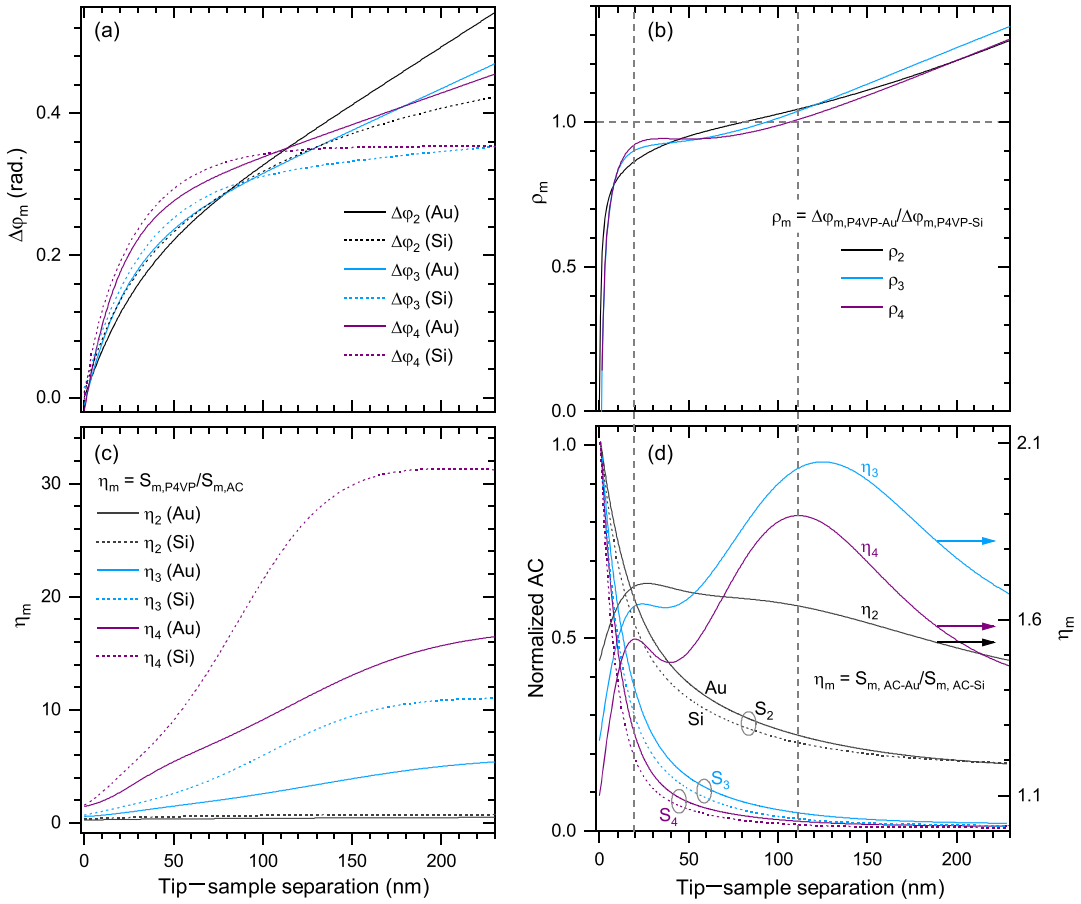


**Figure 3.** (a) Phase changes due to P4VP on Au (solid lines) and Si (dotted lines), (b) Au/Si ratio ($\rho$) of phase changes as a function of P4VP thickness (tip−substrate separation). (c) Near-field amplitude as a function of P4VP thickness divided by the corresponding AC ($S_{m,AC}$) on Au (solid lines) and Si (dotted lines). (d) Left axis: normalized AC on Au (solid lines) and Si (dotted lines). Right axis: Au/Si AC ratio as defined on the plot.

## 3. RESULTS AND DISCUSSION

**3.1. Near-Field Spectra of P4VP.** The near-field optical amplitude ($S_3$) and phase ($\varphi_3$) contrasts of P4VP on gold obtained at different excitation frequencies are displayed in Figure 1d. At all excitation frequencies, a higher near-field amplitude is observed for the bare gold film than for the P4VP coated side because of the higher scattering dielectric properties of the metal. On the other hand, the phase contrast changes drastically with the excitation frequency (see $\varphi_3$ images in Figure 1d). The spectral property of the film is determined by scanning the same area, while tuning the excitation wavenumbers at 2.5 $cm^{-1}$ interval (lower intervals are used to determine the resonance frequency accurately). The variation of the amplitude and phase behaviors due to the polymer is analyzed using the bare substrate as a reference (ref). Accordingly, the relative near-field amplitude ($\eta_m$) and phase difference ($\Delta\varphi_m$) are calculated as

$$\eta_m = \frac{S_{m,P4VP}}{S_{m,ref}} \quad (1)$$

$$\Delta\varphi_m = \varphi_{m,P4VP} - \varphi_{m,ref} \quad (2)$$

The spatially averaged (over 200 nm × 200 nm area) relative amplitude $\eta_3$ and phase difference $\Delta\varphi_3$ using gold surface as a reference are plotted in Figure 1e,f as a function of excitation wavenumber. The reference points used to calculate the average values are indicated by the star symbols on the topography in Figure 1b. The amplitude contrast (Figure 1e) corresponds to the reflection spectrum of the material in the region of the excitation energies. In agreement with reported predictions,[39] the normalized amplitude spectrum has a Lorentzian-derivative-like shape that can be approximated by the real part ($\varepsilon_1$) of the dielectric function ($\varepsilon = \varepsilon_1 + i\varepsilon_2$) of the polymer as shown by the olive-colored line in Figure 1e. On the other hand, the phase difference plotted as a function of excitation wavenumber follows the vibrational absorption spectrum of the polymer, and the trend can be approximated by the imaginary part of the dielectric function as shown by the blue line in Figure 1f. The peak position determined from the near-field phase contrast is in excellent agreement with the far-field FTIR spectrum (red line in Figure 1f), confirming the assignment of the phase contrast at 1598 $cm^{-1}$ to the ring stretching vibration frequency of P4VP. While these are the first near-field result for P4VP, the spectral properties of the amplitude and phase contrasts observed in Figure 1e,f are in good agreement with the results on the intensively investigated PMMA[17,18,39,40,44] and other systems.[19]

**3.2. Thickness-Dependent Near-Field Vibrational Contrast.** Establishing the resonance excitation frequency, we now compare the IR vibrational contrast of the P4VP film on Au and Si substrates at 1598 $cm^{-1}$ ($\lambda$ = 6.26 $\mu$m) laser line using the same AFM tip at the same alignment conditions. The topographic and optical contrasts of the films on the two


https://dx.doi.org/10.1021/acs.jpcc.0c07979
J. Phys. Chem. C 2020, 124, 21018−21026

substrates are displayed in the scan images in Figure 2a,b (see also Figure S1 for the optical images obtained at $m$ = 2 & 4). The corresponding line profiles across the green dashed lines are plotted in Figure 2c,d. From the topography and optical contrasts, it is possible to determine the edge of the P4VP film exactly, as demonstrated in the zoomed-in graphs (see insets in Figure 2c,d). Starting at the edge, as the thicknesses of the films increase almost linearly with 6−8° angle of elevation, the optical amplitude decreases exponentially, as shown by the red lines in Figure 2c,d. On the other hand, the optical phase increases rapidly until the film thickness reaches about 100 nm on both Au and Si substrates (blue lines in Figure 2c,d). As the film thickness increases beyond 100 nm, the phase contrast of P4VP on Au increases approximately linearly, while it appears to saturate on the Si substrate.

For more quantitative comparison, 10 more line profiles that show the variation at different rows across the scan images on Au and Si substrates are extracted (see Figure S2a,b), and the average amplitude and phase signals are plotted as a function of the P4VP thickness that increases the tip−substrate separation (Figure 2e,f). Clearly, the dependence of the phase contrast on the sample thickness is different on the two substrates. Similar to the trend observed in the single line profile as a function of lateral position (Figure 2c,d), the average phase contrast saturates on the Si substrate as the samples becomes thicker than 100 nm, while it continues to increase on Au even as the thickness increases beyond 200 nm.

To facilitate the comparison of the phase contrasts on the two substrates, the trend lines obtained by fitting a biexponential function to the data (solid lines in Figure 2e,f) are plotted in Figure 3a including the results for the $m$ = 2−4 harmonics (the results at each harmonics are compared separately in Figure S3 including the data points). It is interesting to note that for P4VP film thickness smaller than ∼110 nm, the phase contrast increases with $m$ on both substrates as the background suppression becomes more effective. The enhanced optical contrast at higher harmonics is necessary for revealing important details in chemical imaging, as can be seen comparing the optical images obtained at different harmonics (Figure S1) and a representative line profile in Figure S4. The Au/Si ratio ($\rho$) of the P4VP optical phase contrast is less than one up to a film thickness of ∼100 nm in spite of the stronger overall scattering amplitude of the Au substrate than that of Si, as can be seen comparing the scales for the amplitudes in Figure 2c,d. This observation suggests different net field enhancement in the sample supported on Au and Si substrates.

The net field enhancement in the sample can be estimated comparing the near-field amplitude decay as a function of sample thickness to the corresponding approach curve (AC) that measures the amplitude decay when the tip−substrate separation is increased in air. With increasing sample thickness, the amplitude decreases to the limit that the signal strength is determined by the polarizability of the sample assuming that the tip−substrate interaction becomes negligible at a large separation distance. It is shown that the amplitude decay lengths as a function of P4VP thickness on gold (9.5 and 54.1 nm) are smaller than the corresponding decay lengths (10.0 and 64.6 nm) on silicon, as determined by fitting biexponential functions to the third harmonic signal (red solid lines in Figure 2e,f). For example, when the sample thickness increases to 200 nm, the signal decreases to about 19% with respect to bare gold, while it decreases to about 24% with respect to bare silicon. On the other hand, when the tip−substrate separation is increased in air (black lines in Figure 2e,f), the decay lengths on gold (12.1 and 46.2 nm) are larger than the corresponding decay lengths on silicon (8.9 and 37.2 nm). This opposite trend in the near-field amplitude decay on Au and Si as a function of P4VP thickness compared to the tip−substrate separation in air indicates different net field enhancement in the sample on the two substrates. Specifically, the comparison indicates higher net field enhancement for P4VP on Si than on Au, although the overall scattering amplitude is stronger on the Au substrate.

The net field enhancement in the P4VP sample at the tip−substrate junction is approximated by using the AC (field amplitude decay in air) as a reference. As shown in Figure 3c, this approach reveals the field enhancement in the sample as a function of P4VP sample thickness by factoring out the corresponding field decay as a function of tip−substrate separation in air. Note that the curves plotted in Figure 3c show the ratios of the functions with the parameters determined by fitting to the raw data. The fact that the ratios are close to unity for the bare substrates, particularly for $m$ = 4, at which the background suppression is most effective, indicates the stability of the optical alignment throughout the experiment and the validity of using the AC curve as a reference. The results reveal that on both substrates, the net enhancement increases with increasing order of demodulation as the far-field background suppression becomes more effective, consistent with the enhanced optical contrast with increasing order of signal demodulation observed in FigureS 3a and S2c−f. It is also clear that the net enhancement on silicon (dotted lines) is significantly higher than on gold (solid lines) at all harmonics as shown in Figure 3c. In addition, the enhancement tends to saturate with increasing sample thickness on silicon, while it continues to increase on gold, in agreement with the trend of the phase contrast in Figure 2e. However, unlike the phase contrast that crosses as the film thickness increases (Figure 3a), the net enhancement on gold is lower than on silicon at all thicknesses. This observation may indicate a complicated tip−gold substrate optical coupling that includes distance-dependent resonances and strong field gradients.

Some insight into the different nature of probe−substrate optical coupling on gold and silicon may be obtained by analyzing the Au/Si ratios of the ACs. The normalized ACs (left axis in Figure 3d) indicate that the field enhancement decay as a function of tip−substrate distance is faster for Si than for Au as mentioned earlier (the raw data of the ACs is shown in Figurers S2a,b). On both substrates, the signal decays exponentially without any anomaly. However, two peaks are observed in the Au/Si ratio (right axis in Figure 3d), particularly at the 3rd and 4th order harmonics. As the tip−substrate separation increases to 20−24 nm, the ratio increases rapidly and peaks at 24 nm for $m$ = 3 and 20 nm for $m$ = 4, and then, it decreases before it increases again to the second peak at 125 nm for $m$ = 3 and 111 nm for $m$ = 4. Understanding the origin of these peaks requires theoretical modeling, which is beyond the focus of the present work. Similar behavior is observed in the ratio of the phase contrast (Figure 3b), where the ratio of the phase contrast increases rapidly first as the tip−substrate distance increases to 20 nm, which is followed by a slowdown before it increases again approximately linearly.

**3.3. Optical Roughness of the As-Evaporated Gold Surface.** To obtain further insight into the origin of smaller



https://dx.doi.org/10.1021/acs.jpcc.0c07979
J. Phys. Chem. C 2020, 124, 21018−21026

phase contrast for P4VP on gold than on silicon, particularly for ultrathin samples, we compare the topographic and optical images of the bare substrates as shown in Figure 4. The

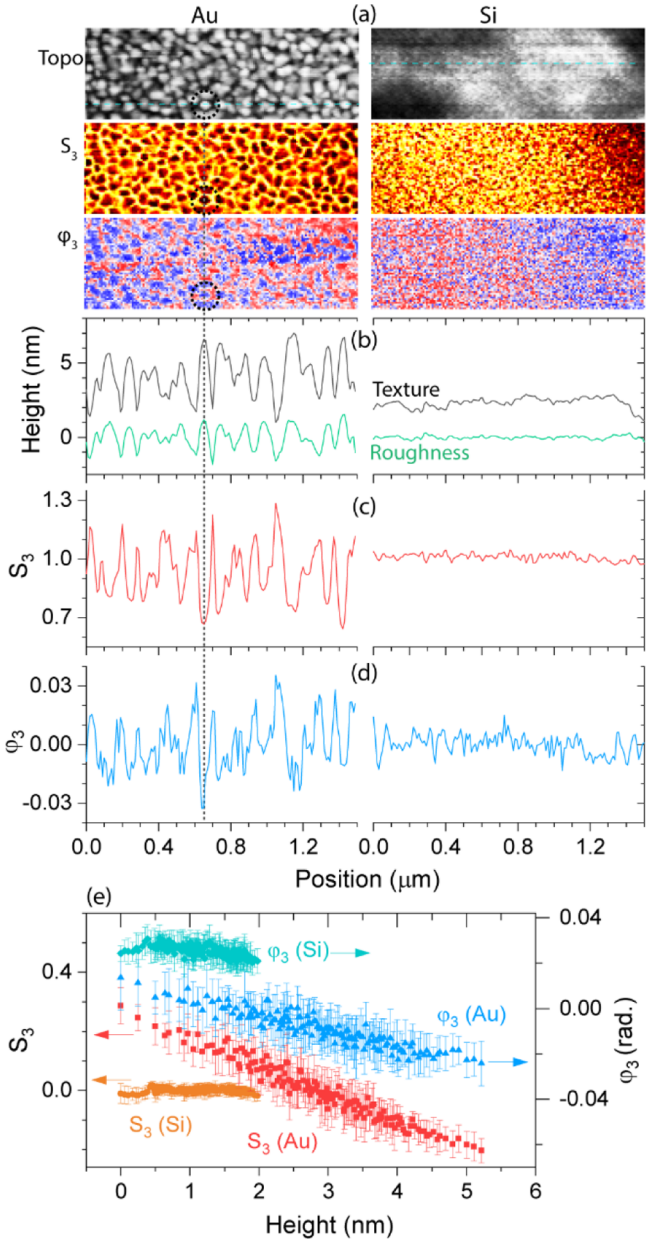


**Figure 4.** Comparison of structural and optical roughness of Au and Si substrates. (a) Topography, near-field amplitude and phase images of bare substrates. (b–d) Representative line profiles showing the structural roughness (b), near-field amplitude (c), and near-field phase (d). High points in the gold film results in low amplitude and phase contrasts as illustrated by the vertical dashed line for the feature in the dotted circle in the topographic and optical images. (e) Average optical amplitude (left axis) and optical phase (right axis) of the bare Au and Si substrate as labeled.

topographic map shows rough surfaces of gold film that is prepared by electron-beam evaporation. The surface roughness of gold reaches up to 1.2 nm, compared to less than 0.3 nm for silicon as estimated from the line profiles plotted in Figure 4b. The amplitude and phase signals confirm that the topographic roughness of gold translates to optical roughness, where the high points in the topography leads to low points in the IR images. The correlation between the topographic height and the IR contrast can be observed more clearly by comparing the line profiles in Figure 4b–d, as illustrated for one of the grain features (circled in the topographic and optical images). As indicated by the vertical dashed line that guides the eyes to correlate the height and the optical contrasts in Figure 4a-d, a peak in the topography (Figure 4b) corresponds to a deep in both IR amplitude (Figure 4c) and phase (Figure 4d) contrast. The correlation between the grain height and IR contrast is further demonstrated in Figure 4e, where the average values of the amplitude (left axis) and phase (right axis) extracted from 10 line profiles are plotted as a function of the topographic height. Clearly, the amplitude and phase values decrease with the height of the gold grains, while on silicon, the contrasts remain approximately constant.

The negative correlation between the grain height and the IR contrast may be explained in terms of the local geometry of the tip–substrate coupling, assuming the grains as small nanoparticles supported on the bulk metal film. As a result, the optical contrast is determined by the tip–particle coupling that intervenes in the interaction of the tip with the bulk film.[45,46] The coupling of the tip to the bulk film can be treated as dipole-image dipole interaction, whereas the tip–particle coupling can be modeled as dipole–dipole interaction. For very small particle sizes, the particle dipoles are smaller than the image dipoles, and the fact that the particles (grains) are intervening between the tip and bulk film reduces the overall scattering amplitude, resulting in contrast reversal.[45]

**3.4. Molecular Near-Field Contrast on Topographically and Optically Rough Surfaces.** To test the effect of the topographic and optical roughness in probing molecular systems with thickness comparable to the surface roughness, the s-SNOM experiment is performed on ultrathin P4VP film with thickness comparable to the surface roughness of gold substrates. A boundary of the P4VP-Au to bare Au is created by immersing and dissolving part of the film in isopropanol for about a second (see Methods). The topography, optical amplitude ($S_3$), and phase ($\varphi_3$) images of the boundary region are shown in Figure 5a. With the exception of some nanoparticles (with height up to 25 nm) possibly created because of solvent-induced polymer aggregation, the film thickness is less than 10 nm (see line profile in Figure S5b). The Au/P4VP-Au boundary is discernible in the optical amplitude and phase images, although the IR contrast due to the P4VP sample is barely above the background fluctuation that originates from the surface roughness (see the line profiles in Figures S5).

In Figure 5b,c, the optical amplitude and phase signals at each pixel are plotted as a function of the topographic height that includes the inherent height variation in the bare gold film. The plots reveal a trimodal distribution, as marked by the vertical dashed lines. The first group ($\lesssim$5 nm) shows the height and optical signal fluctuation within the bare substrate. The second group (5–14 nm) that has the highest density of data points represents the IR contrast due to the ultrathin P4VP film. The scattered data points above 14 nm height are due to relatively large aggregates of the polymer. The trimodal distribution is more apparent in the average values (grouped by topographic height) plotted in Figure 5d,e. Consistent with the results in Figure 4e, the amplitude and phase contrasts decrease as the height within the substrate increases to about 5 nm. As the height further increases because of the P4VP film, the decay rate of the amplitude slows down (Figure 5d), while


https://dx.doi.org/10.1021/acs.jpcc.0c07979
J. Phys. Chem. C 2020, 124, 21018–21026

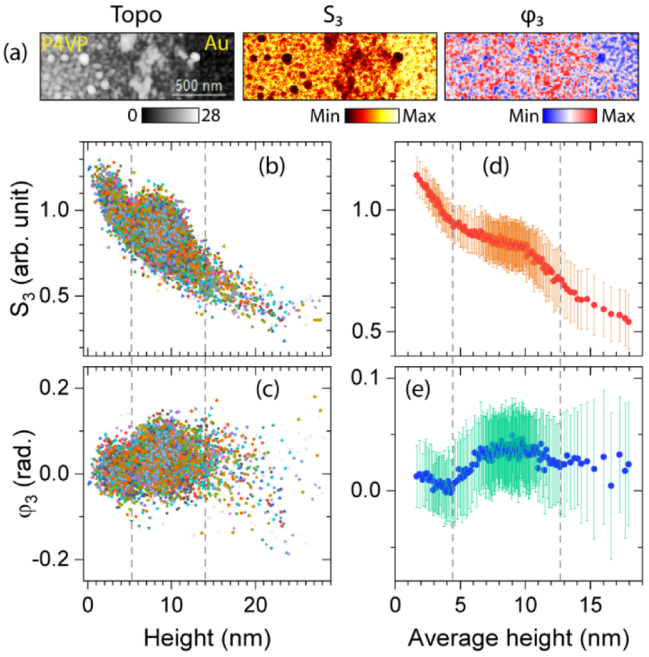


**Figure 5.** s-SNOM contrast due to ultrathin P4VP on the gold surface. (a) Simultaneously obtained topography, optical amplitude ($S_3$), and optical phase ($\varphi_3$) scan images. (b,c) The optical amplitude and optical phase at each pixel in the images are plotted as a function of the topographic height. (d,e) Average s-SNOM amplitude and phase as a function of the average topographic height. The data in each row of pixels are first sorted according to increasing height before the average values are calculated.

the phase contrast on average starts to increase noticeably (Figure 5e). Although the slow-down in the amplitude decay is within the error bars, the general trend may indicate planarization of the surface as the polymer fills the low points of the rough terrain. Overall, comparison of the trends in Figure 5d,e reveals that the phase contrast exhibits more drastic change as the sample thickness increases. However, we note that the contrasts in both amplitude and phase due to the sample are within the background fluctuation. This observation indicates the importance of a topographically and optically smooth substrate for imaging chemicals with molecular thickness.

Relatively smooth gold surface can be obtained using the template striping technique to avoid undefined geometry of tip−sample coupling that results in the fluctuation of optical signal.[19] However, the fact that the phase contrast on silicon is higher than the contrast on gold up to about 100 nm P4VP thickness (Figure 3a,b) and the net field enhancement in the sample is higher on silicon throughout the sample thickness (Figure 3c) suggests that other optical effects are at play on the gold substrate. The rapid initial increase in the Au/Si ratios of the phase contrasts (Figure 3b) and ACs (Figure 3d) may indicate that the contribution of the local coupling effect decreases exponentially as the tip−substrate separation increases. In the long range, the optical contrast should be dominated by the bulk polarizability of the substrate. Therefore, the significantly less field enhancement for the sample on gold than on silicon may indicate absorption of mid-IR radiation by the bulk gold. This should be why the bare gold surface exhibits higher phase contrast than the P4VP-coated surface at off-resonance excitation wavenumbers (1570 and 1620 $cm^{-1}$), as displayed in Figure 1d. Within our excitation frequency range (1570−1620 $cm^{-1}$), the variation of the dielectric function of gold is small (−1435 + i445 to −1350 + i405),[47] but the imaginary (dissipative or absorptive) component is not negligible, which may explain the phase reversal at off-resonance excitation frequencies.

The discussion so far has been focused on the sensitivity of the s-SNOM vibrational imaging as a function of sample thickness based on the bulk property of the P4VP polymer. However, observation of the details of the IR contrasts within the P4VP film indicates variations at the nanoscale. For example, in Figure 5, strong fluctuation of phase contrast is observed for higher than 15 nm sample thickness, which corresponds to the diameter of nanoparticles (aggregates of the polymer). In addition, typical nanoscale dips and peaks have been observed within the P4VP film, particularly on the silicon substrate. These features have been avoided as much as possible in extracting the line profiles in Figures 2 and S2 to characterize the bulk property. Figures S6 and S7 show the variation in the IR contrast due to the local nanoscale features within the P4VP film. Anomalies in the phase contrast are observed within the film, corresponding to high and low points in the topography, as illustrated in Figure S7. In the general trend discussed in Figures 2 and 3, a decrease in the sample height leads to an increase in the optical amplitude and a decrease in the phase contrast. In contrast to this general trend, it is observed that dips in the height leads to peaks in both optical amplitude and phase, and high points in the topography leads to low points in both amplitude and phase contrasts (Figure S7). These anomalies are temporarily attributed to different crystallinity and polarizations of the nanoscale features, which may lead to significant vibrational resonance shift. However, confirming the origin of these anomalies requires obtaining the IR spectra of the nanoscale features, which can be the focus of future studies.

## 4. CONCLUSIONS

In summary, the sensitivity of s-SNOM in chemical imaging using IR radiation is systematically analyzed comparing the near-field vibrational contrast on gold and silicon substrates as a function of P4VP sample thickness. On both substrates, the chemical contrast due to the ring stretching vibration of P4VP changes at the same time as the sample height that increases at a rate of a nanometer per 10 nm lateral displacement crossing from the bare substrate to the P4VP-coated region. Saturation of phase contrast is observed starting at around 100 nm sample thickness on the silicon substrate, while the contrast continues to increase even beyond 200 nm sample thickness on gold. Up to around 100 nm thickness, the net field enhancement in the sample is significantly larger on silicon than on gold in spite of the fact that the overall scattering amplitude is significantly higher on gold. Although the chemical contrast is observable as the sample thickness decreases to a nanometer scale on both gold and silicon substrates, the background fluctuation is significantly larger on gold because of its surface roughness. The variation in the local tip−sample or tip−substrate coupling geometry on the as-evaporated gold surface can lead to background signal fluctuation that can overwhelm the chemical contrast when the sample thickness becomes comparable to the surface roughness. The results presented here may serve as benchmark to search for appropriate substrates to improve the molecular sensitivity of s-SNOM vibrational imaging.


https://dx.doi.org/10.1021/acs.jpcc.0c07979
J. Phys. Chem. C 2020, 124, 21018−21026

## ■ ASSOCIATED CONTENT

### Supporting Information

The Supporting Information is available free of charge at https://pubs.acs.org/doi/10.1021/acs.jpcc.0c07979.

Atomic force microscope topography and mechanical phase, near-field signal, comparison of phase contrast of P4VP on gold and silicon, illustration that more chemical details can be resolved at higher order of demodulation, near-field images and line profiles of ultrathin P4VP film on gold, contrasts of nanoscale features within the P4VP film, and line profiles of the P4VP film (PDF)

## ■ AUTHOR INFORMATION


### Corresponding Author

**Terefe G. Habteyes** − *Center for High Technology Materials and Department of Chemistry and Chemical Biology, University of New Mexico, Albuquerque, New Mexico 87131, United States;* orcid.org/0000-0001-5978-6464; Email: habteyes@unm.edu

### Authors

**Chih-Feng Wang** − *Center for High Technology Materials, University of New Mexico, Albuquerque, New Mexico 87131, United States;* orcid.org/0000-0002-3085-6614

**Bijesh Kafle** − *Center for High Technology Materials and Department of Chemistry and Chemical Biology, University of New Mexico, Albuquerque, New Mexico 87131, United States*

**Tefera E. Tesema** − *Center for High Technology Materials and Department of Chemistry and Chemical Biology, University of New Mexico, Albuquerque, New Mexico 87131, United States*

**Hamed Kookhaee** − *Center for High Technology Materials and Department of Chemistry and Chemical Biology, University of New Mexico, Albuquerque, New Mexico 87131, United States;* orcid.org/0000-0002-0719-3904

Complete contact information is available at: https://pubs.acs.org/10.1021/acs.jpcc.0c07979


### Author Contributions

The manuscript was written through contributions of all authors. All authors have given approval to the final version of the manuscript.

### Notes

The authors declare no competing financial interest.

## ■ ACKNOWLEDGMENTS

This research has been supported by the U.S. National Science Foundation grant no. 1651478. Evaporation of gold was performed at the Center for Integrated Nanotechnologies (CINT), an Office of Science User Facility operated for the U.S. Department of Energy (DOE) Office of Science by Los Alamos National Laboratory (Contract DE-AC52-06NA25396) and Sandia National Laboratories (Contract DE-NA-0003525).

## ■ ABBREVIATIONS

P4VP, poly(4-vinylpyridine); PMMA, poly(methyl methacrylate); s-SNOM, scattering-type scanning near-field optical microscope

## ■ REFERENCES


(1) Inouye, Y.; Kawata, S. Near-Field Scanning Optical Microscope with a Metallic Probe Tip. *Opt. Lett.* **1994**, *19*, 159−161.

(2) Zenhausern, F.; Martin, Y.; Wickramasinghe, H. K. Scanning Interferometric Apertureless Microscopy: Optical Imaging at 10 Angstrom Resolution. *Science* **1995**, *269*, 1083.

(3) Li, J.; Jahng, J.; Pang, J.; Morrison, W.; Li, J.; Lee, E. S.; Xu, J.-J.; Chen, H.-Y.; Xia, X.-H. Tip-Enhanced Infrared Imaging with Sub-10 nm Resolution and Hypersensitivity. *J. Phys. Chem. Lett.* **2020**, *11*, 1697−1701.

(4) Wagner, M.; Jakob, D. S.; Horne, S.; Mittel, H.; Osechinskiy, S.; Phillips, C.; Walker, G. C.; Su, C.; Xu, X. G. Ultrabroadband Nanospectroscopy with a Laser-Driven Plasma Source. *ACS Photonics* **2018**, *5*, 1467−1475.

(5) Wang, H. M.; Wang, L.; Jakob, D. S.; Xu, X. J. G. Tomographic and Multimodal Scattering-Type Scanning near-Field Optical Microscopy with Peak Force Tapping Mode. *Nat. Commun.* **2018**, *9*, 2005.

(6) Kiesow, K. I.; Dhuey, S.; Habteyes, T. G. Mapping Near-Field Localization in Plasmonic Optical Nanoantennas with 10 nm Spatial Resolution. *Appl. Phys. Lett.* **2014**, *105*, 053105.

(7) Huber, A.; Ocelic, N.; Taubner, T.; Hillenbrand, R. Nanoscale Resolved Infrared Probing of Crystal Structure and of Plasmon−Phonon Coupling. *Nano Lett.* **2006**, *6*, 774−778.

(8) Hillenbrand, R.; Keilmann, F.; Hanarp, P.; Sutherland, D. S.; Aizpurua, J. Coherent Imaging of Nanoscale Plasmon Patterns with a Carbon Nanotube Optical Probe. *Appl. Phys. Lett.* **2003**, *83*, 368−370.

(9) Rang, M.; Jones, A. C.; Zhou, F.; Li, Z.-Y.; Wiley, B. J.; Xia, Y.; Raschke, M. B. Optical Near-Field Mapping of Plasmonic Nanoprisms. *Nano Lett.* **2008**, *8*, 3357−3363.

(10) Esteban, R.; Vogelgesang, R.; Dorfmüller, J.; Dmitriev, A.; Rockstuhl, C.; Etrich, C.; Kern, K. Direct Near-Field Optical Imaging of Higher Order Plasmonic Resonances. *Nano Lett.* **2008**, *8*, 3155−3159.

(11) Kim, D.-S.; Heo, J.; Ahn, S.-H.; Han, S. W.; Yun, W. S.; Kim, Z. H. Real-Space Mapping of the Strongly Coupled Plasmons of Nanoparticle Dimers. *Nano Lett.* **2009**, *9*, 3619−3625.

(12) Kim, Z. H.; Leone, S. R. Polarization-Selective Mapping of Near-Field Intensity and Phase around Gold Nanoparticles Using Apertureless Near-Field Microscopy. *Opt. Express* **2008**, *16*, 1733−1741.

(13) Habteyes, T. G. Direct near-Field Observation of Orientation-Dependent Optical Response of Gold Nanorods. *J. Phys. Chem. C* **2014**, *118*, 9119−9127.

(14) Habteyes, T. G.; Dhuey, S.; Kiesow, K. I.; Vold, A. Probe-Sample Optical Interaction: Size and Wavelength Dependence in Localized Plasmon Near-Field Imaging. *Opt. Express* **2013**, *21*, 21607.

(15) Habteyes, T. G.; Staude, I.; Chong, K. E.; Dominguez, J.; Decker, M.; Miroshnichenko, A.; Kivshar, Y.; Brener, I. Near-Field Mapping of Optical Modes on All-Dielectric Silicon Nanodisks. *ACS Photonics* **2014**, *1*, 794−798.

(16) Huth, F.; Govyadinov, A.; Amarie, S.; Nuansing, W.; Keilmann, F.; Hillenbrand, R. Nano-Ftir Absorption Spectroscopy of Molecular Fingerprints at 20 nm Spatial Resolution. *Nano Lett.* **2012**, *12*, 3973−3978.

(17) Pollard, B.; Muller, E. A.; Hinrichs, K.; Raschke, M. B. Vibrational Nano-Spectroscopic Imaging Correlating Structure with Intermolecular Coupling and Dynamics. *Nat. Commun.* **2014**, *5*, 3587.

(18) Mastel, S.; Govyadinov, A. A.; de Oliveira, T. V. A. G.; Amenabar, I.; Hillenbrand, R. Nanoscale-Resolved Chemical Identification of Thin Organic Films Using Infrared Near-Field Spectroscopy and Standard Fourier Transform Infrared References. *Appl. Phys. Lett.* **2015**, *106*, 023113.

(19) Berweger, S.; Nguyen, D. M.; Muller, E. A.; Bechtel, H. A.; Perkins, T. T.; Raschke, M. B. Nano-Chemical Infrared Imaging of Membrane Proteins in Lipid Bilayers. *J. Am. Chem. Soc.* **2013**, *135*, 18292−18295.

(20) Amenabar, I.; Poly, S.; Nuansing, W.; Hubrich, E. H.; Govyadinov, A. A.; Huth, F.; Krutokhvostov, R.; Zhang, L.; Knez,

M.; Heberle, J.; et al. Structural Analysis and Mapping of Individual Protein Complexes by Infrared Nanospectroscopy. *Nat. Commun.* **2013**, *4*, 2890.
(21) Gerber, J. A.; Berweger, S.; O'Callahan, B. T.; Raschke, M. B. Phase-Resolved Surface Plasmon Interferometry of Graphene. *Phys. Rev. Lett.* **2014**, *113*, 055502.
(22) Hu, F.; Luan, Y.; Fei, Z.; Palubski, I. Z.; Goldflam, M. D.; Dai, S.; Wu, J.-S.; Post, K. W.; Janssen, G. C. A. M.; Fogler, M. M.; et al. Imaging the Localized Plasmon Resonance Modes in Graphene Nanoribbons. *Nano Lett.* **2017**, *17*, 5423−5428.
(23) Fei, Z.; Foley, J. J.; Gannett, W.; Liu, M. K.; Dai, S.; Ni, G. X.; Zettl, A.; Fogler, M. M.; Wiederrecht, G. P.; Gray, S. K.; et al. Ultraconfined Plasmonic Hotspots inside Graphene Nanobubbles. *Nano Lett.* **2016**, *16*, 7842−7848.
(24) Fei, Z.; Goldflam, M. D.; Wu, J.-S.; Dai, S.; Wagner, M.; McLeod, A. S.; Liu, M. K.; Post, K. W.; Zhu, S.; Janssen, G. C. A. M.; et al. Edge and Surface Plasmons in Graphene Nanoribbons. *Nano Lett.* **2015**, *15*, 8271−8276.
(25) Dai, S.; Fei, Z.; Ma, Q.; Rodin, A. S.; Wagner, M.; McLeod, A. S.; Liu, M. K.; Gannett, W.; Regan, W.; Watanabe, K.; et al. Tunable Phonon Polaritons in Atomically Thin Van Der Waals Crystals of Boron Nitride. *Science* **2014**, *343*, 1125−1129.
(26) Fali, A.; White, S. T.; Folland, T. G.; He, M.; Aghamiri, N. A.; Liu, S.; Edgar, J. H.; Caldwell, J. D.; Haglund, R. F.; Abate, Y. Refractive Index-Based Control of Hyperbolic Phonon-Polariton Propagation. *Nano Lett.* **2019**, *19*, 7725−7734.
(27) Babicheva, V. E.; Gamage, S.; Zhen, L.; Cronin, S. B.; Yakovlev, V. S.; Abate, Y. Near-Field Surface Waves in Few-Layer $MoS_2$. *ACS Photonics* **2018**, *5*, 2106−2112.
(28) Dai, S.; Ma, Q.; Yang, Y.; Rosenfeld, J.; Goldflam, M. D.; McLeod, A.; Sun, Z.; Andersen, T. I.; Fei, Z.; Liu, M.; et al. Efficiency of Launching Highly Confined Polaritons by Infrared Light Incident on a Hyperbolic Material. *Nano Lett.* **2017**, *17*, 5285−5290.
(29) Ritchie, E. T.; Hill, D. J.; Mastin, T. M.; Deguzman, P. C.; Cahoon, J. F.; Atkin, J. M. Mapping Free-Carriers in Multijunction Silicon Nanowires Using Infrared Near-Field Optical Microscopy. *Nano Lett.* **2017**, *17*, 6591−6597.
(30) Stiegler, J. M.; Huber, A. J.; Diedenhofen, S. L.; Gómez Rivas, J.; Algra, R. E.; Bakkers, E. P. A. M.; Hillenbrand, R. Nanoscale Free-Carrier Profiling of Individual Semiconductor Nanowires by Infrared Near-Field Nanoscopy. *Nano Lett.* **2010**, *10*, 1387−1392.
(31) Choi, W.; Seabron, E.; Mohseni, P. K.; Kim, J. D.; Gokus, T.; Cernescu, A.; Pochet, P.; Johnson, H. T.; Wilson, W. L.; Li, X. Direct Electrical Probing of Periodic Modulation of Zinc-Dopant Distributions in Planar Gallium Arsenide Nanowires. *ACS Nano* **2017**, *11*, 1530−1539.
(32) Jung, L.; Pries, J.; Maß, T. W. W.; Lewin, M.; Boyuk, D. S.; Mohabir, A. T.; Filler, M. A.; Wuttig, M.; Taubner, T. Quantification of Carrier Density Gradients Along Axially Doped Silicon Nanowires Using Infrared Nanoscopy. *ACS Photonics* **2019**, *6*, 1744−1754.
(33) Wang, C.-F.; Habteyes, T. G.; Luk, T. S.; Klem, J. F.; Brener, I.; Chen, H.-T.; Mitrofanov, O. Observation of Intersubband Polaritons in a Single Nanoantenna Using Nano-FTIR Spectroscopy. *Nano Lett.* **2019**, *19*, 4620−4626.
(34) Nikitin, A. Y.; Alonso-González, P.; Vélez, S.; Mastel, S.; Centeno, A.; Pesquera, A.; Zurutuza, A.; Casanova, F.; Hueso, L. E.; Koppens, F. H. L.; et al. Real-Space Mapping of Tailored Sheet and Edge Plasmons in Graphene Nanoresonators. *Nat. Photonics* **2016**, *10*, 239−243.
(35) Xu, Q.; Ma, T.; Danesh, M.; Shivananju, B. N.; Gan, S.; Song, J.; Qiu, C.-W.; Cheng, H.-M.; Ren, W.; Bao, Q. Effects of Edge on Graphene Plasmons as Revealed by Infrared Nanoimaging. *Light: Sci. Appl.* **2017**, *6*, No. e16204.
(36) Jeong, G.; Choi, B.; Kim, D.-S.; Ahn, S.; Park, B.; Kang, J. H.; Min, H.; Hong, B. H.; Kim, Z. H. Mapping of Bernal and Non-Bernal Stacking Domains in Bilayer Graphene Using Infrared Nanoscopy. *Nanoscale* **2017**, *9*, 4191−4195.
(37) Garcia-Etxarri, A.; Romero, I.; de Abajo, F. J. G.; Hillenbrand, R.; Aizpurua, J. Influence of the Tip in Near-Field Imaging of Nanoparticle Plasmonic Modes: Weak and Strong Coupling Regimes. *Phys. Rev. B: Condens. Matter Mater. Phys.* **2009**, *79*, 125439.
(38) Xu, X. G.; Rang, M.; Craig, I. M.; Raschke, M. B. Pushing the Sample-Size Limit of Infrared Vibrational Nanospectroscopy: From Monolayer toward Single Molecule Sensitivity. *J. Phys. Chem. Lett.* **2012**, *3*, 1836−1841.
(39) Taubner, T.; Hillenbrand, R.; Keilmann, F. Nanoscale Polymer Recognition by Spectral Signature in Scattering Infrared Near-Field Microscopy. *Appl. Phys. Lett.* **2004**, *85*, 5064−5066.
(40) Aizpurua, J.; Taubner, T.; García de Abajo, F. J.; Hillenbrand, R.; Hillenbrand, R. Substrate-Enhanced Infrared Near-Field Spectroscopy. *Opt. Express* **2008**, *16*, 1529−1545.
(41) Hauer, B.; Engelhardt, A. P.; Taubner, T. Quasi-Analytical Model for Scattering Infrared Near-Field Microscopy on Layered Systems. *Opt. Express* **2012**, *20*, 13173−13188.
(42) Autore, M.; Mester, L.; Goikoetxea, M.; Hillenbrand, R. Substrate Matters: Surface-Polariton Enhanced Infrared Nanospectroscopy of Molecular Vibrations. *Nano Lett.* **2019**, *19*, 8066−8073.
(43) Ocelic, N.; Huber, A.; Hillenbrand, R. Pseudoheterodyne Detection for Background-Free Near-Field Spectroscopy. *Appl. Phys. Lett.* **2006**, *89*, 101124.
(44) Brehm, M.; Taubner, T.; Hillenbrand, R.; Keilmann, F. Infrared Spectroscopic Mapping of Single Nanoparticles and Viruses at Nanoscale Resolution. *Nano Lett.* **2006**, *6*, 1307−1310.
(45) Kim, Z. H.; Ahn, S.-H.; Liu, B.; Leone, S. R. Nanometer-Scale Dielectric Imaging of Semiconductor Nanoparticles: Size-Dependent Dipolar Coupling and Contrast Reversal. *Nano Lett.* **2007**, *7*, 2258−2262.
(46) Cvitkovic, A.; Ocelic, N.; Aizpurua, J.; Guckenberger, R.; Hillenbrand, R. Infrared Imaging of Single Nanoparticles Via Strong Field Enhancement in a Scanning Nanogap. *Phys. Rev. Lett.* **2006**, *97*, 060801.
(47) Palik, E. D. *Handbook of Optical Constants of Solid*; Elsevier, 1998.


https://dx.doi.org/10.1021/acs.jpcc.0c07979
J. Phys. Chem. C 2020, 124, 21018−21026